

# II-ML: A dimensional analysis-based machine learning parameterization of optical turbulence in the atmospheric surface layer

Maximilian Pierzyna\*

*Faculty of Civil Engineering and Geosciences, Delft University of Technology, Delft, Netherlands*

Rudolf Saathof

*Faculty of Aerospace Engineering, Delft University of Technology, Delft, Netherlands*

Sukanta Basu

*Atmospheric Sciences Research Center, University at Albany, Albany, USA*

(Dated: April 25, 2023)

Turbulent fluctuations of the atmospheric refraction index, so-called optical turbulence, can significantly distort propagating laser beams. Therefore, modeling the strength of these fluctuations ( $C_n^2$ ) is highly relevant for the successful development and deployment of future free-space optical communication links. In this letter, we propose a physics-informed machine learning (ML) methodology, II-ML, based on dimensional analysis and gradient boosting to estimate  $C_n^2$ . Through a systematic feature importance analysis, we identify the normalized variance of potential temperature as the dominating feature for predicting turbulence strength. For statistical robustness, we train an ensemble of models which yields high performance on the out-of-sample data of  $R^2 = 0.958 \pm 0.001$ .

Free-space optical communication (FSOC) between satellites and the ground or between ground-based terminals is among emerging applications in which an optical beam propagates through the atmosphere. FSOC can have a major societal impact, increasing data throughput, data security, and global internet coverage while potentially reducing the cost per bit per second [1]. However, some challenges need to be faced; besides precipitation, clouds, fog, and aerosol scattering, turbulent fluctuations of the atmospheric refractive index form a major source of disturbance for optical beams [2]. The strength of these fluctuations – called optical turbulence – is quantified by the refractive index structure parameter  $C_n^2$ . Good knowledge about the behavior of  $C_n^2$  in diverse locations and meteorological conditions is required to design and deploy reliable future FSOC links. However, measuring  $C_n^2$  is difficult and typically needs elaborate post-processing of high-frequency observations [3]. As a result, a wide range of empirical  $C_n^2$  models and parameterizations have emerged, which aim to relate  $C_n^2$  to more easily obtainable variables [4]. While well-known *models* such as the Hufnagel Valley model yield vertical profiles  $C_n^2(h)$  with little dependency on local meteorological conditions [4], the goal of  $C_n^2$  *parameterizations* is to estimate  $C_n^2$  directly from in-situ measurements.

Conventional physics-based parameterizations typically make use of Monin-Obukhov similarity theory (MOST) [5] and associated empirically determined similarity relationships. One of the earliest parameterizations was proposed by [3] and utilizes turbulent fluxes to estimate  $C_n^2$ . Several other competing formulations exist (refer to [6] for a comprehensive review).

Recently, multiple studies [7–11] showed that ma-

chine learning (ML) models can be used to parametrize  $C_n^2$  based on routinely-available meteorological inputs. These ML approaches are useful from an operational standpoint and can be viewed as sophisticated regression models, but they barely include any physical knowledge. In this letter, we propose an alternative physics-inspired ML framework. We present II-ML, a dimensional analysis-based ML framework, which strives to improve conventional MOST-based parameterizations with the power of ML. We utilize dimensional analysis (DA) constrained with domain knowledge to expand the set of traditional MOST variables and an ensemble of gradient-boosting ML regression models to learn similarity relationships from observations. In DA, the relevant dimensional variables of a physical process are combined into non-dimensional groups that describe that process equally well [12]. DA is compelling to use in practice because the non-dimensional variables enable us to combine observational data from different field campaigns around the world. More importantly, when using ML, DA can change the extrapolation problem in dimensional variables to an interpolation problem in non-dimensional variables [13].

To investigate the strengths and weaknesses of the proposed methodology, we use measurements collected during a seeing study at the Mauna Loa Observatory (MLO) on the island of Hawai'i. The MLO study was conducted by the National Center for Atmospheric Research (NCAR) from 9 June 2006 until 8 August 2006 (~8 weeks). The publicly available dataset contains measurements of mean meteorological quantities, turbulent fluxes, and turbulent variances obtained from three sonic anemometers deployed at ca. 6m, 15m, and 25m height above ground.  $C_n^2$  values were estimated by NCAR using the approach of [14]. We compute two gradients from the mean horizontal wind components  $\bar{u}$  and

---

\* Corresponding author: m.pierzyna@tudelft.nl

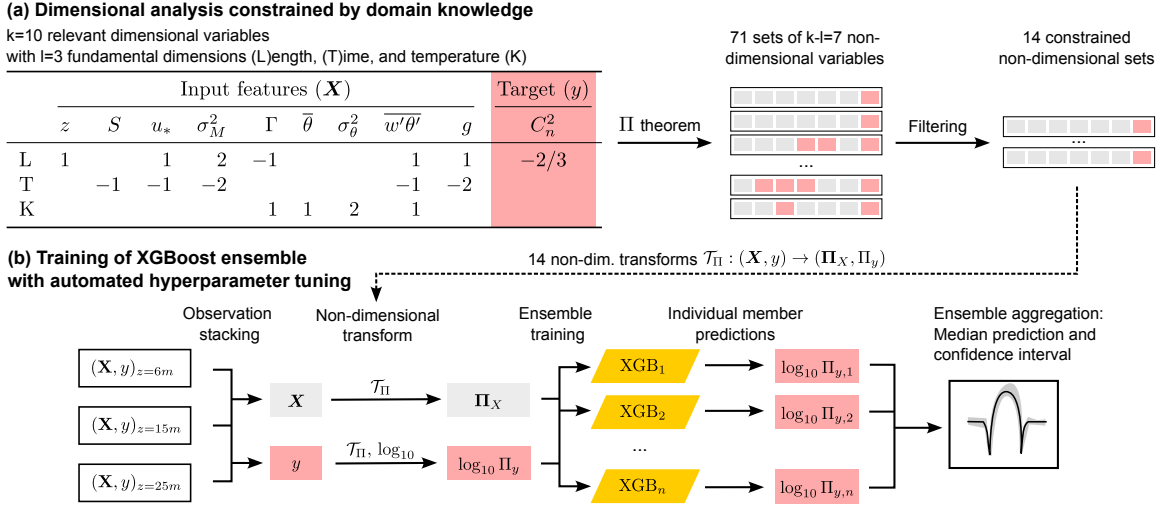


FIG. 1: Our  $\Pi$ -ML methodology consists of two components. (a) The dimensional analysis based on the Buckingham  $\Pi$  theorem combines observed dimensional variables into  $\Pi$  sets of normalized non-dimensional variables. (b) These sets are used to transform the observed data into a stacked non-dimensional dataset to train an ensemble of XGBoost regression models.

$\bar{v}$  and the mean potential temperature  $\bar{\theta}$ : mean wind shear  $S = \sqrt{(\partial\bar{u}/\partial z)^2 + (\partial\bar{v}/\partial z)^2}$  and mean potential temperature gradient  $\Gamma = \partial\bar{\theta}/\partial z$ . Atmospheric turbulence is generated through buoyancy and wind shear, which are captured by the sensible heat flux  $\overline{w'\theta'}$  and the friction velocity  $u_* = \left(\overline{u'w'}^2 + \overline{v'w'}^2\right)^{1/4}$ , respectively, where  $\overline{u'w'}$  and  $\overline{v'w'}$  are momentum flux components. Additionally, we incorporate the variances of potential temperature and horizontal wind magnitude,  $\sigma_\theta^2$  and  $\sigma_M^2 = \sigma_u^2 + \sigma_v^2$ . All relevant variables forming the input for our  $\Pi$ -ML methodology are summarized in the table of figure 1a with their respective fundamental dimensions. For completeness, Earth’s gravitational acceleration  $g = 9.81\text{m s}^{-2}$  is included because it is required for the atmospheric force balance. Given the dry atmospheric conditions at the MLO sites, moisture variables were ignored in the present study but can be included for more humid locations. To later assess the  $C_n^2$  estimation performance of the trained model, the first two weeks of July 2006 are set aside as test data. It is crucial to take the test data out of the middle so that the ML models can capture the seasonal change of meteorology from June to August.

The two key components of our proposed  $\Pi$ -ML methodology are illustrated in figure 1: the DA constrained with domain knowledge (a) and the ensemble of gradient-boosting ML models, which perform regression on the stacked, non-dimensionalized observations (b). The starting point of the DA is the table of variables and dimensions in figure 1a. The Buckingham  $\Pi$  theorem [12], popular in DA, states that our  $k = 10$  dimensional variables with their  $l = 3$  fundamental dimensions (length, time, temperature) can be expressed as a

set of  $(k - l) = 7$  independent non-dimensional  $\Pi$  groups. Multiple options to form the sets exist, so we employ the  $\Pi$  theorem implementation of [15], which generates 71 different sets with 7  $\Pi$  groups each. Using domain knowledge, we conceive the following three constraints to reduce the number of sets from 71 to 14: First, each set can only contain one dependent  $\Pi$  group that is function of  $C_n^2$  (cf. pink highlights in figure 1a). All other  $\Pi$  groups should only be functions of the independent dimensional variables  $\mathbf{X}$ . Second,  $C_n^2$  and its normalized variant  $\Pi_y$  vary over multiple orders of magnitude, so the ML models are trained on  $\log_{10} \Pi_y$ . Since the logarithm is not defined for negative arguments, only  $\Pi$  sets where  $\Pi_y$  is strictly positive are valid. Third, the dimensional variables  $\Gamma$  and  $\overline{w'\theta'}$  can be positive and negative, so raising them to fractional or even-integer powers can result in complex values or a loss of sign. Therefore, valid  $\Pi$  sets cannot contain such expressions. Each of the 14 constrained  $\Pi$  sets is used to scale and non-dimensionalize the dimensional observations  $\mathbf{X}$  and  $y = C_n^2$  to yield  $\Pi_X$  and  $\Pi_y$ , respectively, as illustrated in figure 1b. In their non-dimensional form, the observations from all three levels can be stacked into a combined dataset. From that, ML learns the non-dimensional black box similarity relationship  $f(\Pi_X) \approx \log_{10} \Pi_y$ . For each  $\Pi$  set, we train one ensemble of  $n = 25$  member models to make robust  $C_n^2$  predictions with uncertainty estimates. Each member sees a different 4-week subset of the 6-week training data. The subsets are generated by randomly removing two non-overlapping sets of seven consecutive days from the training data so that each subset covers slightly different meteorological conditions. This is called Monte-Carlo cross-validation. As depicted in figure 1b, each of the  $n$  resulting ensemble members produces a prediction that is robustly aggregated into an ensemble prediction using

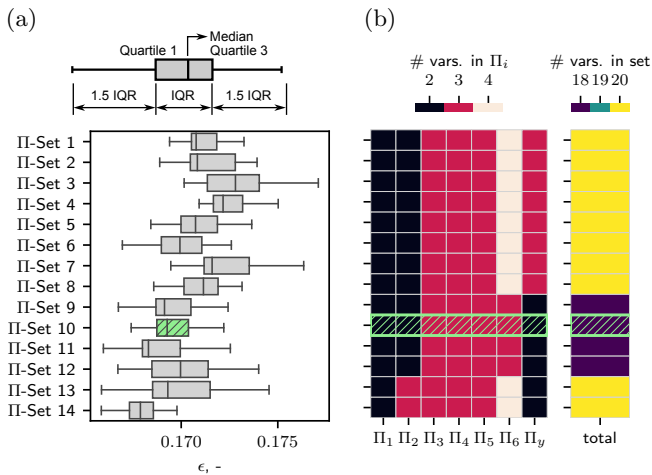


FIG. 2: Comparison of (a) ensemble performance and (b) II set complexity for our 14 different II sets, where winning set 10 (green/hatched) balances performance and complexity well.

the median. The 5-th and 95-th percentiles of the prediction distribution correspond to 90% confidence bounds. Each member model is trained separately on its respective 4-week training data subset using the gradient boosting algorithm XGBoost (XGB) and the AutoML library FLAML [16]. FLAML performs time-constrained hyperparameter tuning of the XGB models using 5-fold cross-validation. For this study, for each member, FLAML was given a 10-minute time budget on 8 cores of a 3 GHz Intel Xeon E5-6248R CPU. Such a time-constrained optimization is crucial to keep the computational costs of training one 25-member ensemble reasonable ( $\sim 34$  core hours).

The prediction accuracy and model complexity of each trained II-ML ensemble is assessed to decide which II set is best suited for our ML-based optical turbulence similarity theory. The root-mean-squared error (RMSE)  $\epsilon = \sqrt{\langle (y - \hat{y})^2 \rangle}$  in the *dimensional* log-space is utilized to quantify accuracy as the deviation between the observed  $\log_{10} C_n^2 = y$  from the test set (July 1 – 14) and the corresponding *dimensional* II-ML prediction  $\hat{y} = \log_{10} \hat{C}_n^2$ . We also evaluate the complexity of the II sets and their trained ML ensembles. That is essential because ML models should only be as complex as necessary to increase their ability to perform well on new unseen data [17]. One II set is considered simpler than another set if its II groups are constructed from fewer dimensional variables. Similarly, one trained ensemble is considered simpler than another one if fewer II groups are important for the ML prediction, i.e. the modeled  $C_n^2$  is sensitive to fewer input features. The features importance of the trained II-ML models is obtained with the permutation feature importance technique (PFI) [18, 19]. For each feature  $\Pi_i$ , PFI yields a ratio  $(\epsilon_i' - \epsilon)/\epsilon$  which describes how the RMSE  $\epsilon_i'$  of a trained model magnifies when the model gets decorrelated data for  $\Pi_i$  compared to the baseline RMSE  $\epsilon$  where the correlation is intact.

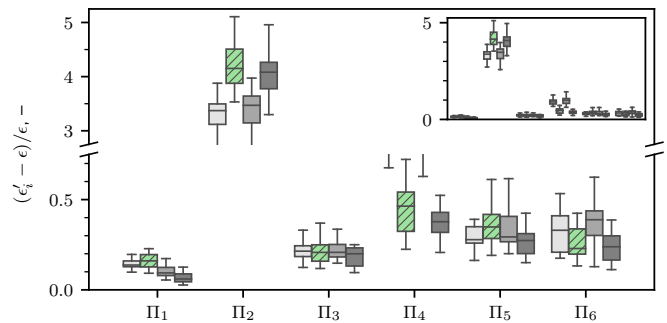


FIG. 3: Importance of non-dimensional II groups for II-ML ensembles 9, 10, 11, and 12 (left to right) based on the permutation feature importance strategy. The best performing ensemble 10 is marked in green (hatched).

That means a highly important feature result in a large error magnification. The interested reader is referred to [19] for a more detailed description of PFI.

The performance and complexity of the 14 II-ML ensembles are shown in figure 2. The boxplots in panel (a) display the  $\epsilon$  distributions for each ensemble as illustrated in the sketch above the plots. While all ensembles show median RMSEs of the same magnitude, II sets 9 to 14 outperform the others. Panel (b) visualizes complexity through the number of dimensional variables constituting each II group (left) together with the sum per set (right). This plot reveals that sets 9 to 12 of the well-performing ensembles are the only ones consisting of II groups formed from no more than three dimensional variables. The winning ensemble out of these four low-error low-complexity candidates is selected based on the PFI score distributions displayed in figure 3. Remember that the DA yields different functional expressions for  $\Pi_i$  for each set, which is why each set shows different PFI distributions. The boxplots reveal that II sets 9 and 11 result in more complex II-ML ensembles compared to 10 and 12 because they significantly rely on two II groups ( $\Pi_2$  and  $\Pi_4$ , see inset) for  $C_n^2$  estimation instead of one ( $\Pi_2$ ). Consequently, only sets 10 and 12 remain candidates for our ML-based similarity theory of optical turbulence. Because of the lower  $\epsilon$  spread in figure 2a, we select II-ML ensemble 10 with  $\Pi_1 = \sigma_M^2/u_*^2$ ,  $\Pi_2 = \bar{\theta}/\sqrt{\sigma_\theta^2}$ ,  $\Pi_3 = (Sz)/u_*$ ,  $\Pi_4 = \overline{w'\theta'}/(u_*\sigma_\theta)$ ,  $\Pi_5 = (gz)/u_*$ ,  $\Pi_6 = (\Gamma z)/\sigma_\theta$ , and  $\Pi_y = (C_n^2)^{3/2} z$ . The expressions for the other 13 II sets can be found in appendix A. The observation that  $\Pi_2$  – the inverse of the normalized potential temperature variance – is the only dominating feature of our parameterization has important practical implications: First, temperature variances can be measured with thermocouples [20], which are cheaper than sonic anemometers. Second, the low relevance of the gradients ( $\Pi_3$  and  $\Pi_6$ ) indicates that even single-level measurements might be sufficient to estimate  $C_n^2$  accurately. Therefore, our approach might lead to simpler  $C_n^2$  measurement setups.

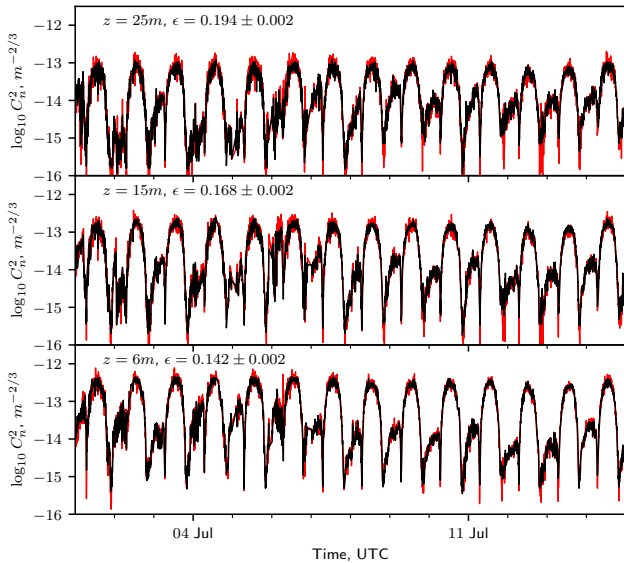


FIG. 4: Median predictions of  $\log_{10} C_n^2$  based on test data (black) using the selected II set 10 ensemble. The observed values (red) are shown for reference.

The performance of the final II-ML ensemble is illuminated in more detail in figures 4 and 5. The observed (red) and the predicted median evolutions of  $C_n^2$  (black) for the test data are shown in figure 4. The evolutions are plotted for the three original sonic heights individually for visualization. The agreement between prediction and observation is high for all levels, although the level-specific  $\epsilon$  slightly increases with height. It is assumed that processes higher in the atmosphere force the turbulence underneath, which would be missed by the sonics and, thus, our ensemble. Notable errors on all levels mostly occur during atmospheric neutral conditions – shortly after sunrise and sunset – where our ensemble overestimates the observed  $C_n^2$  drops to  $10^{-15}$  and lower. This behavior is also visible in the 2D correlation histogram of figure 5a and the quantile-quantile (QQ) plot in 5b. Panel (a) directly compares observed  $C_n^2$  samples to their ML-estimated counterpart, while panel (b) plots the cumulative density functions of observed and estimated  $C_n^2$  against each other. The overestimation of neutral conditions is visible in both panels as the deviation of the histogram/curve from the ideal 1:1 line (dashed) for  $C_n^2 < 10^{-15}$ . Simultaneously, the grey 90% confidence band in (b) grows, which indicates increasing disagreement between the predictions of the ensemble members. However, less than 8% of  $C_n^2$  measurements are smaller than  $10^{-15}$ , so the regularization of the ML training results in models that favor the center of the  $C_n^2$  distribution, not its tails. Also, the lower signal-to-noise ratio of the sonic anemometers in weak turbulence conditions increases the measurement uncertainty. Since very low turbulence conditions are also not critical for optical applications such as optical links or astronomy, we argue that little emphasis should be put on these devia-

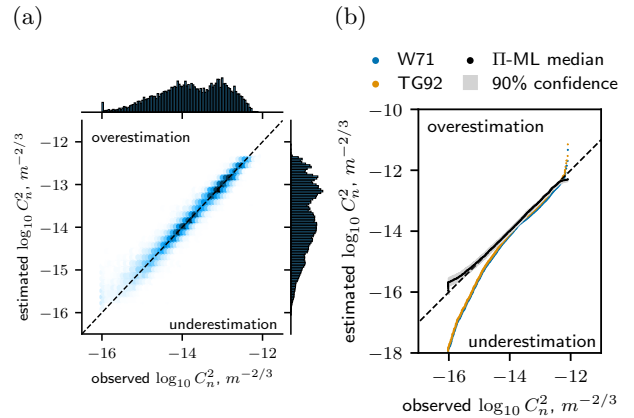


FIG. 5: Correlation histogram and quantile-quantile plot for II set 10 ensemble showing (a) high correlation ( $R^2 = 0.958 \pm 0.001$ ) and (b) well-captured  $C_n^2$  distributions compared to traditional models from literature (blue, orange).

tions. The regularization mentioned above also explains the minor underestimation visible in panel (b) for observations with  $C_n^2 > 10^{-12.5}$ , which make up less than 3.5% of the data. Leaving the tails of the distributions aside, both panels of figure 5 show excellent performance of our ensemble for most data. Most points in (a) the histogram and (b) the QQ plot are close to the ideal 1:1 line as quantified by the coefficient of determination of  $R^2 = 0.958$  computed on all test data, including the deviating tails. The spread of the correlation distribution around the 1:1 line is symmetric for  $C_n^2 > 10^{-15}$ . That means the ensemble predictions are well-balanced and not biased towards over or underestimation for most of the  $C_n^2$  range. A brief comparison of II-ML with two conventional MOST-based  $C_n^2$  parameterizations (W71 [3] and TG92 [21]) in figure 5b illustrates the potential of improvement by utilizing ML. While W71 and TG92 have the operational advantage of being formulated as analytical equations, they lack the flexibility to capture non-linear behavior where ML excels. This results in the larger over and underestimations shown in the QQ plots.

In summary, we demonstrated how dimensional analysis constrained with domain knowledge yields non-dimensional scaling expressions, which enable us to train accurate XGBoost regression models. While the methodology was applied in this letter to optical turbulence, it can be applied to model physical processes of all kinds. From an optics perspective, our approach has two advantages over  $C_n^2$  parameterizations from literature: First, the final ensemble produced highly accurate predictions during day and night, while previous models are often limited to one or the other [4]. Second, the non-dimensional formulation allows making predictions with a pre-trained ensemble for new sonics set up at different heights or locations as long as the climatology is similar. That is not possible with previous ML-based models. Our final II-ML ensemble was shown to perform well, regardless

of the complex meteorology of Hawaii and the limited measurement duration of only two months. While the complexity and data sparsity of the MLO campaign limits the applicability of the trained ensemble to other sites, the good performance leads us to assume that our II-ML methodology works equally well or better in more favorable setups. Additionally, we observed a strong dependency of  $C_n^2$  on  $\sigma_\theta^2$  ( $\Pi_2$ ), suggesting that cheaper single-level variance measurements might be sufficient for accurate  $C_n^2$  estimation. In conclusion, we presented a powerful, statistically robust physics-informed machine learning methodology (II-ML) to estimate  $C_n^2$  from turbulence measurements.

## ACKNOWLEDGMENTS

MP is financed by the FREE project (P19-13) of the TTW-Perspectief research program partially financed by the Dutch Research Council (NWO).

### Appendix A: Full list of non-dimensional II set expressions

Table I provides a full list of the non-dimensional expressions of the 14 II sets as shown in figure 2. The  $\Pi_i$  groups are sorted by complexity just like in figure 2b, and the normalized  $C_n^2$  target is denoted  $\Pi_y$ .

- 
- [1] H. Hemmati, *Near-Earth Laser Communications* (CRC Press, 2009).
  - [2] H. Kaushal and G. Kaddoum, Optical Communication in Space: Challenges and Mitigation Techniques, *IEEE Communications Surveys & Tutorials* **19**, 57 (2017), arxiv:1705.10630 [cs, math].
  - [3] J. C. Wyngaard *et al.*, Behavior of the Refractive-Index-Structure Parameter near the Ground\*, *Journal of the Optical Society of America* **61**, 1646 (1971).
  - [4] F. G. Smith *et al.*, *Atmospheric Propagation of Radiation*, The Infrared & Electro-Optical Systems Handbook, Vol. 2 (Infrared Information Analysis Center, 1993).
  - [5] A. S. Monin and A. M. Obukhov, Basic laws of turbulent mixing in the surface layer of the atmosphere, *Contrib. Geophys. Inst. Acad. Sci.* **151** (1954).
  - [6] M. J. Savage, Estimation of evaporation using a dual-beam surface layer scintillometer and component energy balance measurements, *Agricultural and Forest Meteorology* **149**, 501 (2009).
  - [7] Y. Wang and S. Basu, Using an artificial neural network approach to estimate surface-layer optical turbulence at Mauna Loa, Hawaii, *Optics Letters* **41**, 2334 (2016).
  - [8] C. Jellen *et al.*, Machine learning informed predictor importance measures of environmental parameters in maritime optical turbulence, *Applied Optics* **59**, 6379 (2020).
  - [9] C. Jellen *et al.*, Machine-learning informed macro-meteorological models for the near-maritime environment, *Applied Optics* **60**, 2938 (2021).
  - [10] L. A. Bolbasova *et al.*, The application of machine learning to predictions of optical turbulence in the surface layer at Baikal Astrophysical Observatory, *Monthly Notices of the Royal Astronomical Society* **504**, 6008 (2021).
  - [11] C. Su *et al.*, In situ measurements and neural network analysis of the profiles of optical turbulence over the Tibetan Plateau, *Monthly Notices of the Royal Astronomical Society* **506**, 3430 (2021).
  - [12] P. K. Kundu *et al.*, *Fluid Mechanics*, 5th ed., Vol. 1 (Academic Press, 2012).
  - [13] K. Kashinath *et al.*, Physics-informed machine learning: Case studies for weather and climate modelling, *Philosophical Transactions of the Royal Society A: Mathematical, Physical and Engineering Sciences* **379**, 20200093 (2021).
  - [14] S. Oncley and T. Horst, *Calculation of Cn2 for Visible Light and Sound from CSAT3 Sonic Anemometer Measurements*, Tech. Rep. (2013).
  - [15] M. Karam and T. Saad, BuckinghamPy: A Python software for dimensional analysis, *SoftwareX* **16**, 100851 (2021).
  - [16] C. Wang *et al.*, FLAML: A Fast and Lightweight AutoML Library (2021), arxiv:arXiv:1911.04706.
  - [17] V. N. Vapnik, *Statistical Learning Theory*, Adaptive and Learning Systems for Signal Processing, Communications, and Control (Wiley, New York, 1998).
  - [18] L. Breiman, Random Forest, *Machine Learning* **45**, 5 (2001).
  - [19] C. Molnar, *Interpretable Machine Learning: A Guide for Making Black Box Models Explainable*, second edition ed. (Christoph Molnar, Munich, Germany, 2022).
  - [20] J. D. Albertson *et al.*, Sensible Heat Flux From Arid Regions: A Simple Flux-Variance Method, *Water Resources Research* **31**, 969 (1995).
  - [21] V. Thiermann and H. Grassl, The measurement of turbulent surface-layer fluxes by use of bichromatic scintillation, *Boundary-Layer Meteorology* **58**, 367 (1992).

TABLE I: Expressions of all non-dimensional  $\Pi$  sets for features ( $\Pi_i$ ) and respective target variable  $\Pi_y$  (scaled  $C_n^2$ ). Note that  $\sigma_X$  denotes the standard deviations of quantity  $X$  related to the variance  $\sigma_X^2$  as  $\sigma_X = \sqrt{\sigma_X^2}$ . The final set selected for its balance of ensemble prediction accuracy and complexity is marked with (\*).

Set	$\Pi_1$	$\Pi_2$	$\Pi_3$	$\Pi_4$	$\Pi_5$	$\Pi_6$	$\Pi_y$
Set 1	$\frac{\sigma_M^2}{u_*^2}$	$\frac{\sigma_\theta^2}{\theta^2}$	$\frac{S z}{u_*}$	$\frac{w' \theta'}{\theta u_*}$	$\frac{g}{S u_*}$	$\frac{\Gamma u_*}{S \theta}$	$\frac{u_* (C_n^2)^{3/2}}{S}$
Set 2	$\frac{\sigma_M^2}{u_*^2}$	$\frac{\bar{\theta}}{\sigma_\theta}$	$\frac{S z}{u_*}$	$\frac{w' \theta'}{u_* \sigma_\theta}$	$\frac{g}{S u_*}$	$\frac{\Gamma u_*}{S \sigma_\theta}$	$\frac{u_* (C_n^2)^{3/2}}{S}$
Set 3	$\frac{\sigma_M^2}{u_*^2}$	$\frac{\sigma_\theta^2}{\theta^2}$	$\frac{g z}{u_*^2}$	$\frac{S u_*}{g}$	$\frac{w' \theta'}{\theta u_*}$	$\frac{\Gamma u_*^2}{g \theta}$	$\frac{u_*^2 (C_n^2)^{3/2}}{g}$
Set 4	$\frac{\sigma_M^2}{u_*^2}$	$\frac{\bar{\theta}}{\sigma_\theta}$	$\frac{g z}{u_*^2}$	$\frac{S u_*}{g}$	$\frac{w' \theta'}{u_* \sigma_\theta}$	$\frac{\Gamma u_*^2}{g \sigma_\theta}$	$\frac{u_*^2 (C_n^2)^{3/2}}{g}$
Set 5	$\frac{u_*}{\sigma_M}$	$\frac{\sigma_\theta^2}{\theta^2}$	$\frac{S z}{\sigma_M}$	$\frac{w' \theta'}{\theta \sigma_M}$	$\frac{g}{S \sigma_M}$	$\frac{\Gamma \sigma_M}{S \theta}$	$\frac{\sigma_M (C_n^2)^{3/2}}{S}$
Set 6	$\frac{u_*}{\sigma_M}$	$\frac{\bar{\theta}}{\sigma_\theta}$	$\frac{S z}{\sigma_M}$	$\frac{w' \theta'}{\sigma_\theta \sigma_M}$	$\frac{g}{S \sigma_M}$	$\frac{\Gamma \sigma_M}{S \sigma_\theta}$	$\frac{\sigma_M (C_n^2)^{3/2}}{S}$
Set 7	$\frac{u_*}{\sigma_M}$	$\frac{\sigma_\theta^2}{\theta^2}$	$\frac{g z}{\sigma_M^2}$	$\frac{S \sigma_M}{g}$	$\frac{w' \theta'}{\theta \sigma_M}$	$\frac{\Gamma \sigma_M^2}{g \theta}$	$\frac{\sigma_M^2 (C_n^2)^{3/2}}{g}$
Set 8	$\frac{u_*}{\sigma_M}$	$\frac{\bar{\theta}}{\sigma_\theta}$	$\frac{g z}{\sigma_M^2}$	$\frac{S \sigma_M}{g}$	$\frac{w' \theta'}{\sigma_\theta \sigma_M}$	$\frac{\Gamma \sigma_M^2}{g \sigma_\theta}$	$\frac{\sigma_M^2 (C_n^2)^{3/2}}{g}$
Set 9	$\frac{\sigma_M^2}{u_*^2}$	$\frac{\sigma_\theta^2}{\theta^2}$	$\frac{S z}{u_*}$	$\frac{w' \theta'}{\theta u_*}$	$\frac{g z}{u_*^2}$	$\frac{\Gamma z}{\theta}$	$(C_n^2)^{3/2} z$
Set 10*	$\frac{\sigma_M^2}{u_*^2}$	$\frac{\bar{\theta}}{\sigma_\theta}$	$\frac{S z}{u_*}$	$\frac{w' \theta'}{u_* \sigma_\theta}$	$\frac{g z}{u_*^2}$	$\frac{\Gamma z}{\sigma_\theta}$	$(C_n^2)^{3/2} z$
Set 11	$\frac{u_*}{\sigma_M}$	$\frac{\sigma_\theta^2}{\theta^2}$	$\frac{S z}{\sigma_M}$	$\frac{w' \theta'}{\theta \sigma_M}$	$\frac{g z}{\sigma_M^2}$	$\frac{\Gamma z}{\theta}$	$(C_n^2)^{3/2} z$
Set 12	$\frac{u_*}{\sigma_M}$	$\frac{\bar{\theta}}{\sigma_\theta}$	$\frac{S z}{\sigma_M}$	$\frac{w' \theta'}{\sigma_\theta \sigma_M}$	$\frac{g z}{\sigma_M^2}$	$\frac{\Gamma z}{\sigma_\theta}$	$(C_n^2)^{3/2} z$
Set 13	$\frac{\sigma_\theta^2}{\theta^2}$	$\frac{u_*}{\sqrt{g} \sqrt{z}}$	$\frac{S \sqrt{z}}{\sqrt{g}}$	$\frac{\sigma_M^2}{g z}$	$\frac{\Gamma z}{\theta}$	$\frac{w' \theta'}{\sqrt{g} \theta \sqrt{z}}$	$(C_n^2)^{3/2} z$
Set 14	$\frac{\bar{\theta}}{\sigma_\theta}$	$\frac{u_*}{\sqrt{g} \sqrt{z}}$	$\frac{S \sqrt{z}}{\sqrt{g}}$	$\frac{\sigma_M^2}{g z}$	$\frac{\Gamma z}{\sigma_\theta}$	$\frac{w' \theta'}{\sqrt{g} \sigma_\theta \sqrt{z}}$	$(C_n^2)^{3/2} z$